ACS APPLIED MATERIALS & INTERFACES

www.acsami.org

Research Article

Reaction Kinetics and Mass Transfer Synergistically Enhanced Electrodes for High-Performance Zinc−Bromine Flow Batteries

Jiayi Li,[†] Zeyu Xu,[†] and Maochun Wu*

Cite This: *ACS Appl. Mater. Interfaces* 2025, 17, 25206−25215

Read Online

ACCESS | Metrics & More | Article Recommendations | Supporting Information

ABSTRACT: Zinc−bromine flow batteries (ZBFBs) hold great promise for grid-scale energy storage owing to their high theoretical energy density and cost-effectiveness. However, conventional ZBFBs suffer from inhomogeneous zinc deposition and sluggish Br_2/Br^- redox kinetics, resulting in a short cycle life and low power density. Herein, a multiscale porous electrode with abundant nitrogen-containing functional groups is developed by growing zeolitic imidazolate framework-8 in situ on graphite felts, followed by a facile carbonization process to simultaneously tackle both the challenges. Theoretical and experimental results reveal that nitrogen-containing functional groups exhibit a high adsorption energy toward zinc atoms, while the microstructures promote pore-level mass transport, thereby resulting in compact and uniform zinc deposition. In the meantime, the electrode boosts the Br_2/Br^- reaction kinetics due to its high catalytic activity and large surface area. As a result, the ZBFBs equipped with optimized electrodes at both negative and positive sides can operate at an ultrahigh current density of 250 mA cm^{-2} while maintaining an energy efficiency of 68.0%, far surpassing that with pristine graphite felts (50.7%). Remarkably, the battery exhibits excellent cycling stability over 2000 cycles without obvious decay. This study provides a simple yet effective method for developing high-performance electrodes to tackle the critical challenges in ZBFBs, thereby promoting the commercialization of this promising energy storage technology.

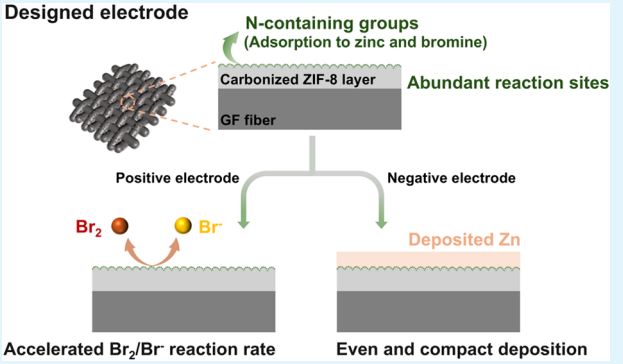

KEYWORDS: *zinc−bromine flow batteries, zinc dendrite, phase field simulation, multiscale electrode, reaction kinetics*

1. INTRODUCTION

Shifting from fossil fuels to renewable energy sources, particularly solar and wind, is essential to achieving carbon neutrality.[1,2] Nevertheless, the inherent fluctuating nature of these renewables requires large-scale energy storage to maintain grid stability.[3,4] Of various technologies, aqueous flow batteries have garnered much attention owing to their distinct attributes such as inherent safety, site flexibility, and exceptional scalability.[5−7] In particular, ZBFBs stand out as one of the most attractive candidates because of their high theoretical specific energy (440 Wh kg^{-1}), high cell potential (~1.85 V), and the use of inexpensive and widely available materials.[8,9] Despite these advantages, the practical application of ZBFBs is hindered by their limited operating current density and short cycle life.[10,11] The former primarily results from sluggish Br_2/Br^- reaction kinetics on the positive electrode, while the latter is due to dendrite formation and "dead Zn" associated with shedding issues on the negative side, which considerably jeopardizes the efficiency and longevity of ZBFBs.[12−15]

Electrodes, which offer not only active sites for electrochemical reactions but also ion/mass transport pathways, play a key role in determining the performances of ZBFBs.[16,17] Currently, carbon-based materials, especially graphite felts (GFs), are common electrode materials for ZBFBs owing to their superior electrical conductivity, high stability, high porosity, and low cost.[18−20] However, conventional GFs only offer a limited active surface for electrochemical reactions due to the smooth, highly graphitized fiber surface. When used as negative electrodes, the smooth fiber surface results in few Zn deposition sites and insufficient adhesion to the Zn deposits. Consequently, the deposited Zn tends to grow into dendrites and easily falls off with the flow of electrolyte during charging and discharging processes, greatly reducing Coulombic efficiencies (CEs) and shortening the cycle life of ZBFBs.[21] When applied as positive electrodes, ZBFBs suffer from large polarizations, leading to low energy efficiencies (EEs) and limiting operating current density.[4] In the past, tremendous efforts have been devoted to tackling these challenges by modifying the electrode surface properties. For negative

Received: December 18, 2024
Revised: April 8, 2025
Accepted: April 11, 2025
Published: April 18, 2025

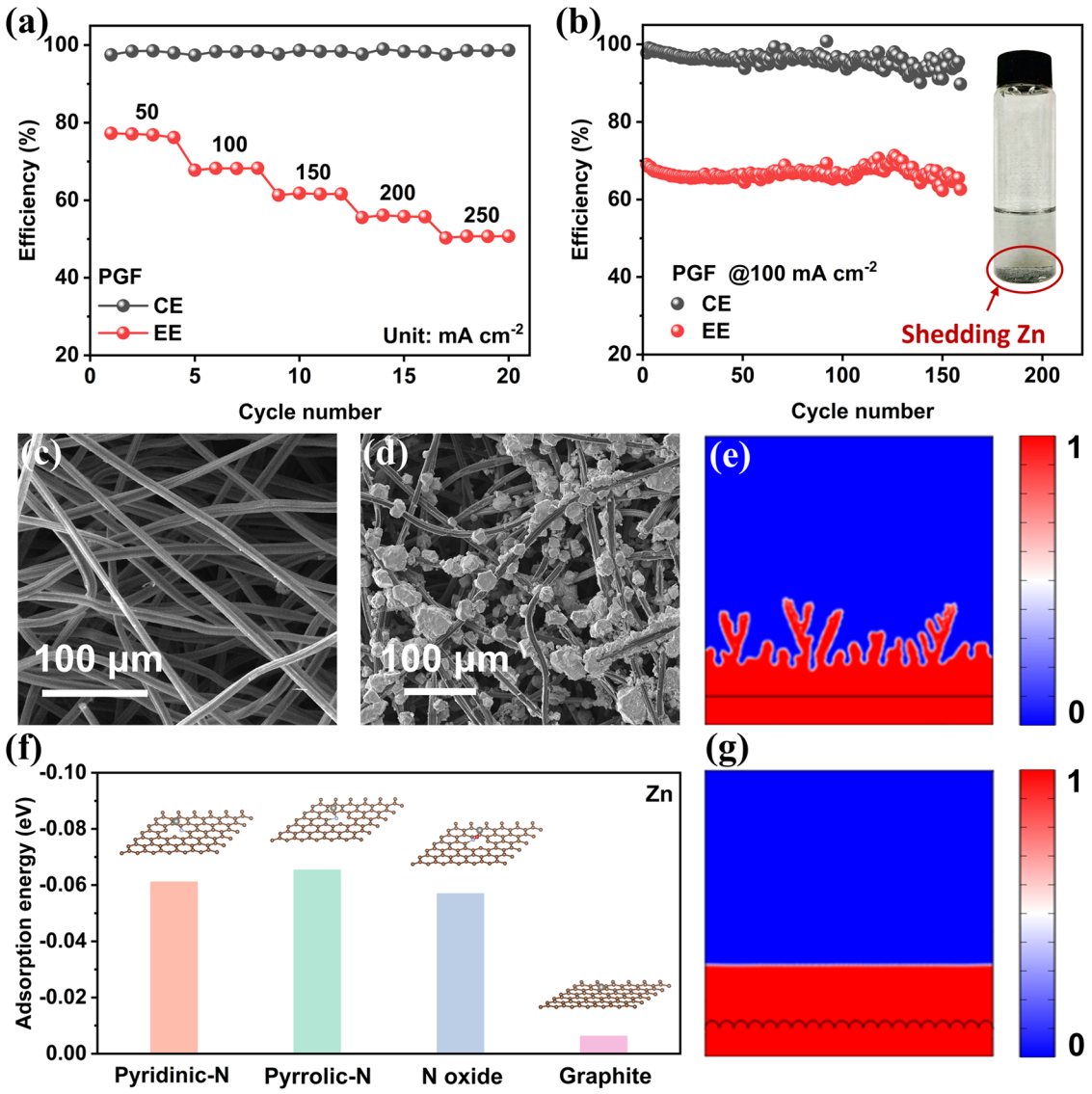

Figure 1. (a) CE and EE of ZBFB using PGF as both positive and negative electrodes at different current densities. (b) Zn shedding in the electrolyte tank and cycling performance of ZBFB with PGF electrodes at 100 mA cm^{-2}. SEM image of (c) PGF and (d) Zn deposited on the PGF negative electrode on the membrane side after 12 min of charge at 100 mA cm^{-2}. (e) Phase field simulation of Zn deposition on the PGF electrode surface. (f) Adsorption energy of zinc atoms on different electrode surfaces. (g) Phase field simulation of Zn deposition on the designed electrode surface.

electrodes, Sun et al. and Lee et al. demonstrated that the single-vacancy carbon defect presents high bonding energy with Zn and can prevent surface diffusion of Zn, thus effectively suppressing Zn dendrite growth.[22,23] Lu et al. reported that incorporating N-rich defects into electrodes significantly increases the Zn adsorption capacity while creating more nucleation sites for Zn deposition.[21] Additionally, Yin et al. developed a tin (Sn)-deposited carbon felt to achieve uniform Zn plating/stripping thanks to the strong Zn−Sn interaction and enhanced hydrogen evolution overpotential of Sn.[24] As for the positive side, major efforts were mainly focused on improving the electrochemical activity of conventional GFs for the Br_2/Br^- reaction by heteroatom (e.g., oxygen[20] and nitrogen[25]) doping and application of electrocatalysts (e.g., platinum,[26] titanium nitride,[12] and carbon nanotube[27]). Despite the tremendous progress, the performance of ZBFBs still remains inferior, particularly when compared to that of its all-vanadium counterpart. This is because most previous studies mainly focused on solving only one specific issue, rendering the overall performance unsatisfactory. Therefore, it remains a great challenge to develop electrodes that can simultaneously address Zn dendrite formation and sluggish Br_2/Br^- reaction kinetics.

Herein, a nitrogen-doped, multiscale porous electrode was designed and fabricated to simultaneously address both challenges in ZBFBs. Density functional theory (DFT) calculations reveal that the N-containing functional groups provide high affinity toward Zn atoms and bromine molecules, thus promoting compact zinc deposition and enhancing Br_2/Br^- conversion rates. Phase field simulation further unravels that the microstructured surface effectively promotes dendrite-free deposition due to the enhanced interfacial mass transport. It is demonstrated that the ZBFBs equipped with the newly designed positive and negative electrodes are capable of operating at an ultrahigh current density of 250 mA cm^{-2} with an EE of 68.0% and show no obvious degradation for 2000 cycles at 100 mA cm^{-2}, whereas the battery with pristine graphite felt (PGF) electrodes delivers an EE of as low as 50.7% at 250 mA cm^{-2} and

https://doi.org/10.1021/acsami.4c22329
ACS Appl. Mater. Interfaces 2025, 17, 25206−25215

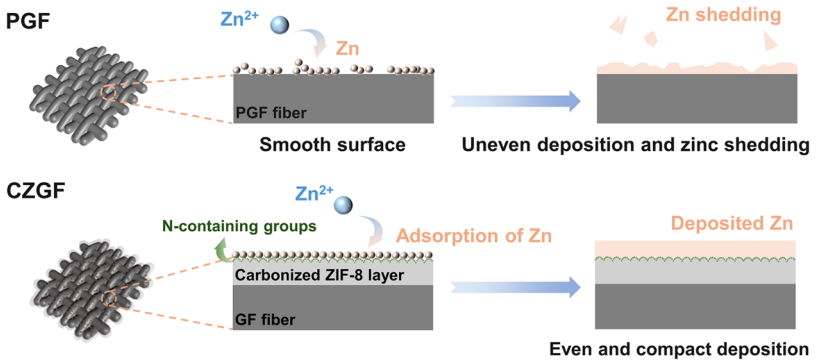

Figure 2. Schematic Illustrations of Zn Deposition on PGF and Designed CZGF Electrodes.

suffers from fluctuation only after about 50 cycles at 100 mA cm^{-2}.

2. RESULTS AND DISCUSSION

Figure 1a shows the rate performance of ZBFB assembled with PGF electrodes. It is found that even at a low current density of 50 mA cm^{-2}, the EE is only about 76.2% and continues dropping to 50.7% when the current density reaches 250 mA cm^{-2}, indicating the high polarization resulting primarily from low electrochemical activity of PGFs. Cycling test in Figure 1b further reveals that the CE of ZBFB decreases significantly and then becomes unstable after around 50 cycles at 100 mA cm^{-2}. Meanwhile, shedding Zn was observed in both the negative electrolyte tank and tube. This is due to the nonuniform Zn deposition and some Zn may be flushed away by the flowing electrolyte due to the insufficient binding of Zn and electrode, which is consistent with previous works.[28−30] To better understand the origin of shedding Zn, surface morphologies before and after Zn deposition were observed by scanning electron microscopy (SEM). As shown in Figure 1c, PGF exhibits a smooth fiber surface that can provide only limited active sites for Zn deposition. As expected, the deposited Zn on PGF is nonuniform in both size and spatial distribution (Figure 1d) after being charged at 100 mA cm^{-2} for 12 min (corresponding to 20 mAh cm^{-2}). It can be presumed that the adhesion between Zn grains and fiber surfaces is weak, which could easily lead to Zn abscission, thus decreasing the CE and cycle stability of ZBFBs. Phase field simulations were then conducted to reveal the underlying mechanism of dendrite formation. As shown in Figure 1e and Video S1, during the electrodeposition process, the electrode−electrolyte interface moves toward the electrolyte and becomes rough. Further growth of these unevenly deposited Zn results in rampant dendrite formation. During the discharge process, these dendrites are prone to break and fall off from the electrode surface during the dissolution process to form "dead zinc", which is flushed away by the flowing electrolyte, resulting in low CE and poor stability.

To gain insights into the shedding of Zn, DFT calculations were carried out to study the interaction of Zn atoms with the pristine graphite surface (Figure 1f). It was found that the absorption energy is as low as −0.006 eV, indicating the weak adsorption between Zn and pristine electrode, which is a root cause of Zn shedding during battery operation. An effective solution to address this issue is to design a surface that exhibits a high binding energy toward Zn atoms. As heteroatom doping is one of the most promising methods to modulate the surface properties, we calculated the adsorption energies of *N*-containing defects toward Zn atoms, which are −0.061, −0.065, and −0.057 eV for pyridinic-*N*, pyrrolic-*N*, and *N* oxide, respectively, which are much more negative than that on the pristine graphite surface. The lone pair electrons of these *N*-containing groups can coordinate with Zn^{2+}, reducing the nucleation energy barrier and promoting uniform nucleation.[31−33] These results indicate N-doping is a promising way to enhance the adsorption ability to Zn atoms, which is conducive to anchoring Zn and thus promotes compact Zn deposition. Moreover, additional charge carriers introduced by *N*-containing groups can enhance the uniform distribution of electric field on the electrode surface, thereby alleviating local current concentration that may lead to uneven Zn deposition.[34]

In addition to the surface properties that largely determine the nucleation process, uniform ion distribution at the electrode/electrolyte surface is critical to dendrite-free Zn deposition.[35,36] We conjecture that constructing microprotrusions on the smooth fiber surface will promote mass transfer at the interface, thus suppressing dendrite growth. Phase field simulation was then performed to preliminarily validate this hypothesis. Numerical results in Figure 1g and Video S2 reveal that the protrusions formed during the electrode modification process are indeed beneficial to the flat, uniform, and dendrite-free Zn formation. This is attributed to the fact that the rough surface promotes the uniform distribution and transfer of Zn^{2+} ions at the electrode/electrolyte interface.[37]

Guided by the above fundamental understanding, a N-doped, multiscale porous electrode was proposed by carbonizing ZIF-8 in situ growth on GFs (CZGFs). As illustrated in Figure 2, when using PGF as a negative electrode, which has fewer and uneven Zn nucleation sites, the Zn deposit is uneven and prone to shedding. By contrast, the designed CZGF electrode with a rough N-containing layer derived from carbonized ZIF-8 not only provides abundant sites with strong adsorption for Zn nucleation but also enhances the interfacial mass transfer of Zn^{2+} ions due to the increased surface flow velocity (Figure S1), thereby achieving uniform and dense Zn deposition. Figure S2 illustrates the synthesis procedure of the CZGFs. First, PGF was immersed in a mixed solution of $Zn(NO_3)_2{\cdot}6H_2O$ and 2-methylimidazole for in situ growth of ZIF-8 particles. As the carbonization temperature is a key parameter that determines the removal of Zn during pyrolysis and significantly influences structural and compositional properties of the resulting electrodes, the ZIF-8-modified GFs (ZGFs) were then carbonized at 700, 800, 900, and 1000 °C for 5 h under the N_2 atmosphere to achieve different CZGFs (denoted as CZGF-700, CZGF-800, CZGF-900, and CZGF-1000).

https://doi.org/10.1021/acsami.4c22329
ACS Appl. Mater. Interfaces 2025, 17, 25206−25215

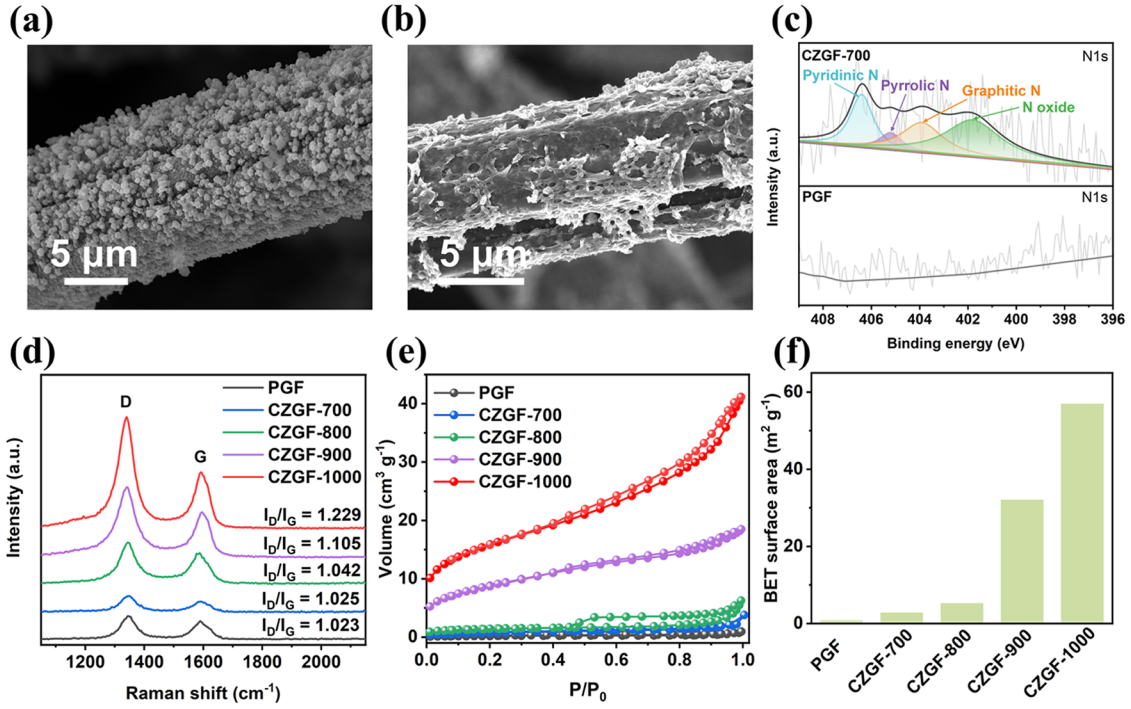

Figure 3. SEM images of (a) ZGF and (b) CZGF-700 electrode surfaces. (c) N 1s XPS spectra of CZGF-700 and PGF. (d) Raman spectra, (e) nitrogen adsorption−desorption isotherms, and (f) BET surface area of different electrodes.

SEM images in Figures 3a and S3 show that the PGF fiber surface is uniformly coated with rhombic polyhedral ZIF-8 particles after soaking in the precursor solution. X-ray diffractometer (XRD) patterns in Figure S4a reveal that the ZGF shows typical diffraction peaks corresponding to the (011), (002), (112), (022), (013), and (222) crystal planes of ZIF-8, confirming successful growth of ZIF-8 on PGF.[38,39] After carbonization under a N_2 atmosphere at 700 °C, the ZIF-8 nanoparticles disappear and are transformed into a rough carbon layer coated on the surface of GF fibers (Figure 3b). This is because ZIF-8 particles undergo partial decomposition at 600 °C and are fully transformed to carbon at 700 °C, which is evidenced by the shift in the XRD patterns of CZGF-700 shown in Figure S4b. During this process, the decomposition of ZIF-8 results in the formation of carbon with ZnO, simultaneously facilitating the formation of porous structures.[40] SEM images of CZGFs obtained under various carbonization temperatures are shown in Figure S5. It is found that as the carbonization temperature increases, the particle size in the carbonized ZIF-8 layer gradually decreases. This may be due to the fact that the higher carbonization temperature will intensify the pyrolysis process, enabling reduction of ZnO and evaporation of Zn to form a more porous and defect-rich structure.[23] Then, the composition and elemental chemical states of the prepared electrodes were analyzed by X-ray photoelectron spectroscopy (XPS). Full XPS spectra survey (Figures S6 and S7a) reveals that the carbonization of ZIF-8 successfully incorporates *N*-containing functional groups to the electrodes. As shown in Figures 3c and S7b, the N 1s spectrum is deconvoluted to four peaks located at 398.6, 399.8, 401.1, and 403.2 eV, which correspond to pyridinic-*N*, pyrrolic-*N*, graphitic-*N*, and *N* oxide, respectively.[41] These *N*-containing functional groups are beneficial to increasing the adsorption ability to Zn atoms and thus promote uniform and robust Zn deposits. Raman spectra were also acquired to probe the surface properties of CZGFs. As displayed in Figure 3d, all samples exhibit two typical peaks. One centered at ∼1342 cm^{-1} is the D band that is associated with the disordered carbon or other carbon defects, while the other located at ∼1590 cm^{-1} corresponds to the G band related to graphitic carbon. In general, the amount of defects in the carbon materials was characterized by the intensity ratio of D to G band (I_D/I_G).[42] The values of I_D/I_G for PGF, CZGF-700, CZGF-800, CZGF-900, and CZGF-1000 are calculated to be 1.023, 1.025, 1.042, 1.105, and 1.229, respectively. As the temperature increases, nitrogen atoms gradually decompose or volatilize, leaving behind vacancies and edge defects in the carbon lattice.[43] These defects contribute to an increase in I_D/I_G, leading to a higher I_D/I_G ratio, despite the overall graphitization trend. Moreover, Zn vaporization above 908 °C creates pores, further amplifying disordered carbon domains and enhancing the surface area of electrodes.[44−46] Figure 3e displays the N_2 adsorption−desorption isotherms of different electrodes. It is found that the adsorption capacity of the electrode increases with an increasing carbonization temperature. Moreover, the hysteretic loop of the CZGF-1000 electrode can be classified to type IV, which reveals the existence of numerous mesopores and micropores and is further verified by the pore size distribution in Figure S8.[47] Figure 3f depicts that the Brunauer−Emmett−Teller (BET) surface area increases with the carbonization temperature. Thanks to the presence of these meso- and micropores, the specific surface area dramatically increases from 0.72 m^2 g^{-1} for PGF to 56.91 m^2 g^{-1} for CZGF-1000, thereby considerably increasing the reaction sites.

To experimentally validate our hypothesis of the designed electrodes for dendrite-free Zn deposition, a ZBFB was assembled with CZGF-700 as the negative electrode and PGF as the positive electrode and cycled at 100 mA cm^{-2}. The results show that the ZBFB can cycle stably for over 800 cycles without obvious degradation, and no detached Zn is observed in the electrolyte tank and tubes (Figure 4a), confirming the

https://doi.org/10.1021/acsami.4c22329
ACS Appl. Mater. Interfaces 2025, 17, 25206−25215

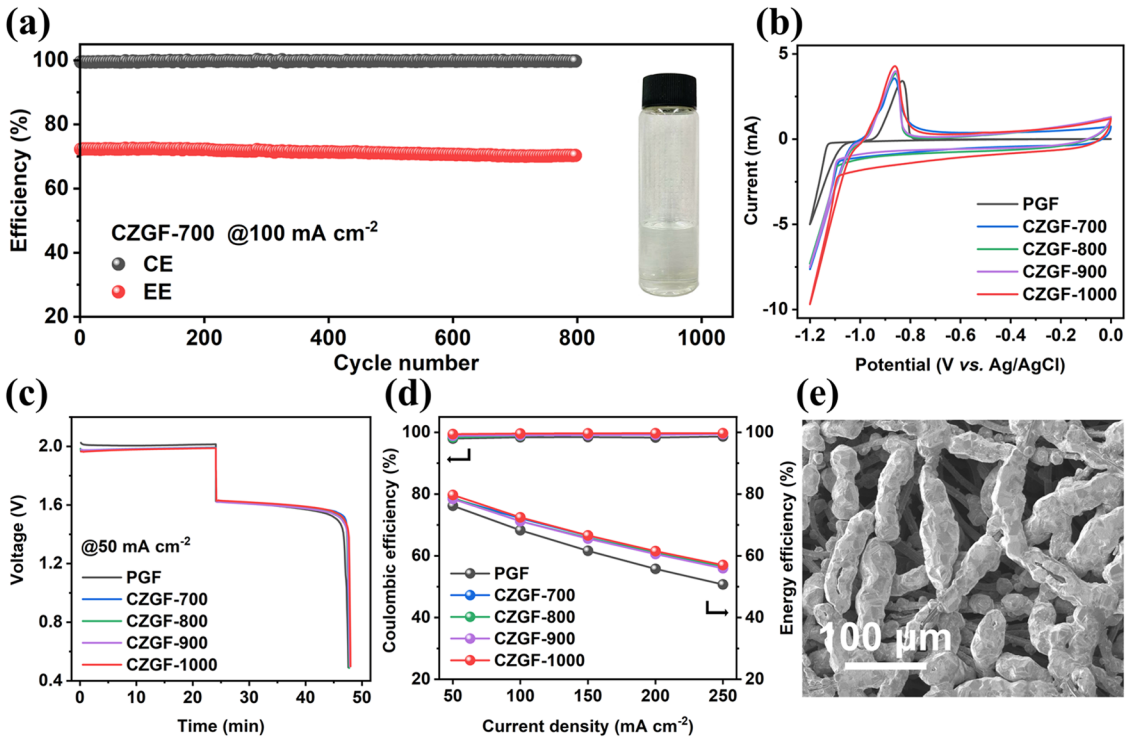

Figure 4. (a) Cycling performance of ZBFB using CZGF-700 and PGF as negative and positive electrodes at 100 mA cm^{-2} and the negative electrolyte after cycling. (b) CV profiles of different samples at a scan rate of 10 mV s^{-1}. (c) Charge−discharge profiles of ZBFBs with different CZGF negative electrodes and the same PGF positive electrodes at 50 mA cm^{-2}. (d) CE and EE of ZBFBs with various negative electrodes and the same PGF positive electrodes at different current densities. (e) SEM image of Zn deposited on the CZGF-1000 negative electrode on the membrane side after 12 min of charge at 100 mA cm^{-2}.

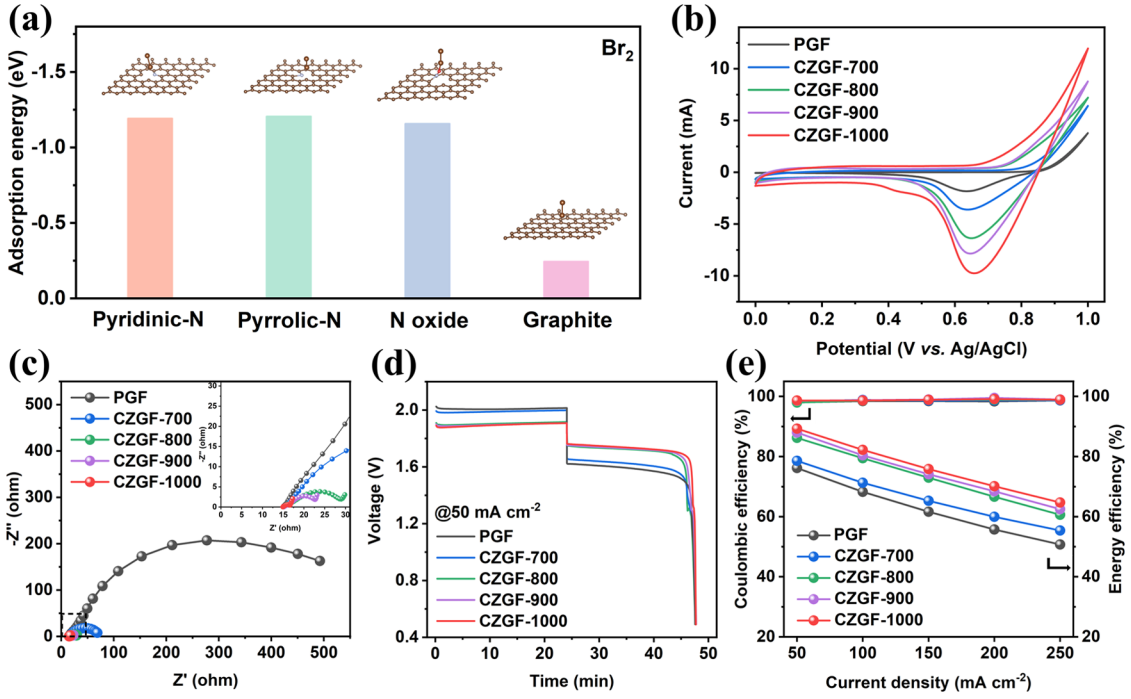

Figure 5. (a) Adsorption energy of bromine on representative surfaces of CZGF and PGF. (b) CV profiles of different electrodes with the potential ranging from 0 to 1 V vs. Ag/AgCl. (c) Nyquist plots of different samples. (d) Voltage−time profiles of ZBFBs with different positive electrodes during the charge−discharge processes at 50 mA cm^{-2}. (e) CE and EE of ZBFBs with different positive electrodes when charged and discharged at various current densities.

effectiveness of our strategy in tackling the critical challenge of Zn electrodes. The cyclic voltammetry (CV) test was then performed to evaluate the Zn deposition/dissolution behavior on different electrodes. As displayed in Figures 4b and S9, the

https://doi.org/10.1021/acsami.4c22329
ACS Appl. Mater. Interfaces 2025, 17, 25206−25215

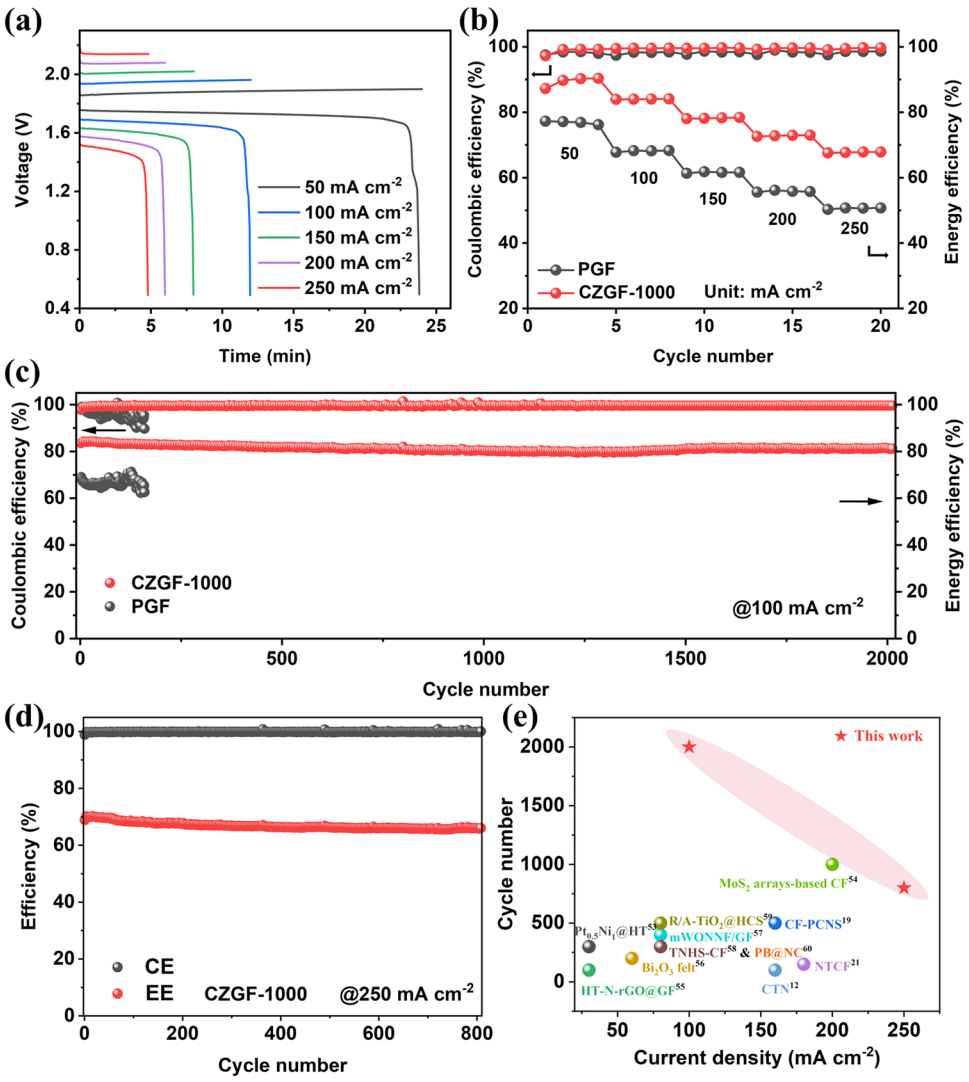

Figure 6. (a) Voltage−time profiles and (b) CE and EE of ZBFBs using CZGF-1000 as both negative and positive electrodes at different current densities. (c) Cycling performances of ZBFBs with both PGF and CZGF-1000 electrodes at 100 mA cm^{-2} and 20 mAh cm^{-2}. (d) Cycling performance with both CZGF-1000 electrodes at 250 mA cm^{-2} and 20 mAh cm^{-2}. (e) Comparison of operating current density and cycling number of ZBFBs using CZGF-1000 electrodes with recently reported related works.[12,19,21,53−60]

initial Zn deposition potentials on PGF, CZGF-700, CZGF-800, CZGF-900, and CZGF-1000 are −1.146, −1.100, −1.106, −1.104, and −1.103 V, respectively. The difference in the initial deposition overpotential of zinc on different CZGF electrodes is not obvious. However, the initial Zn deposition potential with CZGFs changes positively and the deposition overpotential is reduced by about 43 mV compared to the PGF, demonstrating that a smaller Zn deposition barrier needs to be overcome,[48] which facilitates the uniform deposition of Zn.[49,50] All cathodic currents and anodic peak currents of CZGFs are higher than those of PGF. As the carbonization temperature increases, the anodic peak current gradually increases, and CZGF-1000 shows the highest results among all tested electrodes. Moreover, the anodic peak potential of CZGFs shifts negatively compared with PGF, indicating a certain increase in reversibility for the Zn^{2+}/Zn reactions. In addition, ZBFBs were also assembled to assess the effect of using modified CZGFs as negative electrodes on the battery performance. The charge−discharge voltage curves of ZBFBs with various CZGF negative electrodes and the same PGF positive electrodes were compared in Figure 4c. It is found that replacing PGF with CZGF as a negative electrode reduces charge voltage plateaus and improves discharge voltage plateaus of ZBFBs. There is no obvious difference in the charge and discharge voltage plateaus of ZBFBs using varied CZGF negative electrodes, indicating the carbonization temperature has no significant effect on the Zn^{2+}/Zn reaction kinetics. Figure 4d displays the CEs and EEs of the ZBFBs tested under different current densities. Encouragingly, the batteries installed with the CZGF negative electrodes exhibit high CEs exceeding 99.2%, which is about 1% higher than that with PGF. This is primarily ascribed to the improved Zn deposition. The ZBFB with the CZGF-1000 negative electrode also exhibits exceptional cycling stability at 100 mA cm^{-2} with no obvious performance degradation after about 800 cycles (Figure S10). As shown in Figure 4e, dense, compact Zn electrodeposits are found on CZGFs, which fully cover the fiber surface. Although EEs are also improved when CZGFs are used as negative electrodes, probably due to the slightly enhanced reaction kinetics or increased surface area, the improvement is limited and the EEs are relatively low (~56.6%) when operated at a high current density of 250 mA cm^{-2}. It is inferred that the larger polarization mainly comes from the positive electrode,[51] which will be

https://doi.org/10.1021/acsami.4c22329
ACS Appl. Mater. Interfaces 2025, 17, 25206−25215

addressed in the following section. More remarkably, when deposited at a higher areal capacity of 40 mAh cm^{-2}, CZGF-1000 can still maintain a uniform and flat Zn deposition (Figure S11), whereas Zn is unevenly deposited on the surface of PGF. These results successfully confirm that the newly designed CZGF electrodes can effectively induce dendrite-free Zn deposition, thereby greatly extending the cycle life of ZBFBs.

As mentioned above, the sluggish Br_2/Br^- reaction kinetics is another critical barrier hindering the development of ZBFBs. Inspired by the unique features of *N*-containing functional groups, DFT calculations were performed to examine their adsorption capability toward bromine molecules. As shown in Figure 5a, all *N*-containing groups exhibit lower adsorption energies than the pristine carbon surface due to the fact that these *N*-containing groups contain more electrons and have a strong adsorption capacity for bromine molecules, which are more inclined to gain electrons, resulting in a much faster rate of the Br_2/Br^- reaction.[19] CV tests were subsequently conducted to evaluate the Br_2/Br^- reaction kinetics using CZGF electrodes. Figure 5b shows that the cathodic peak currents and oxidation currents of CZGFs are higher than those of PGF in the CV curves, suggesting the improved electrode activity. With the carbonization temperature increasing, the cathodic peak current also increases and the highest cathodic peak current is obtained with CZGF-1000 due to its largest active surface area among these CZGFs. Electrochemical impedance spectroscopy (EIS) tests further elucidated the electrochemical processes occurring on different electrodes. Nyquist plots in Figure 5c and the equivalent circuit in Figure S12 reveal that the bulk solution resistances (R_s) with PGF and CZGFs are around 15 Ω, indicating little difference in electrical conductivity for these samples, while the semicircle diameters exhibit a progressive reduction in the order of PGF > CZGF-700 > CZGF-800 > CZGF-900 > CZGF-1000, suggesting the reduced charge transfer resistance (R_{ct}) with CZGFs. This also confirms that the CZGF-1000 electrode possesses the fastest kinetics toward Br_2/Br^- reactions among all modified CZGFs, consistent with the CV results.

ZBFBs with different positive electrodes and PGF negative electrodes were then assembled to further evaluate their electrochemical performances. As shown in Figure 5d, a sequential reduction in charge voltage plateau in the order of PGF > CZGF-700 > CZGF-800 > CZGF-900 > CZGF-1000 is observed, while the discharge plateau increases in the reverse trend. Accordingly, the ZBFB assembled with the CZGF-1000 positive electrode delivers the highest EE of 89.3% at 50 mA cm^{-2}, far outperforming that with PGF electrodes (76.2%). This is primarily ascribed to enhanced reaction kinetics and surface area of CZGF-1000 electrodes. The EE and CEs of ZBFBs with different positive electrodes operating from 50 to 250 mA cm^{-2} are summarized in Figure 5e. The CEs display an increase trend with increasing current density, primarily attributed to reduced bromine crossover, while reduced EEs result from increased polarization under elevated current densities.[52] The ZBFBs with modified CZGF positive electrodes exhibit higher EEs than that with PGF electrode under all tested current densities, indicating the fast reaction kinetics of the Br_2/Br^- couple. Remarkably, the CZGF-1000 positive electrode enables ZBFB to achieve a high EE of 64.7% even at 250 mA cm^{-2}, confirming the excellent rate performance.

Eventually, the performances of ZBFBs with both positive and negative CZGF-1000 electrodes were evaluated with increasing current densities. The resulting charge−discharge curves presented in Figure 6a show that as the current density increases, the gaps between the charge and discharge voltage increase as a result of the increased polarizations. Additionally, the performances of ZBFBs with both PGF and CZGF-1000 operated at different current densities are presented in Figure S13. It is clearly seen that the gaps between the charging and discharging plateaus of the ZBFB with CZGF-1000 electrodes are smaller than those with PGF, thus leading to a much higher EE. Figure 6b presents the corresponding CEs and EEs of the ZBFBs with both the CZGF-1000 and PGF electrodes. The results show that the CEs of battery using CZGF-1000 electrodes reach 99.7% as a result of dendrite-free Zn deposition, which are higher than that with PGF electrodes. Impressively, ZBFB installed with CZGF-1000 electrodes exhibits an ultrahigh EE of 90% at 50 mA cm^{-2} and can still maintain an EE of 68.0% at 250 mA cm^{-2}, far surpassing that equipped with PGF electrodes. To assess the durability of CZGFs, the ZBFBs with CZGF-1000 as both negative and positive electrodes were cycled at different current densities. The results in Figure 6c show that the ZBFB can maintain an EE above 81% over 2000 stable cycles (over 800 h) when operated at 100 mA cm^{-2}. Notably, even at 250 mA cm^{-2}, the ZBFB still exhibits exceptional stability over 800 cycles (Figure 6d), which exceeds the performance reported in most previous works on ZBFBs shown in Figure 6e and Table S1. In addition, the polarization test was conducted, and the result is shown in Figure S14. It is found that the ZBFB with CZGF-1000 electrodes can deliver a maximum power density of as high as 707.6 mW cm^{-2}, far surpassing that with PGFs (432.4 mW cm^{-2}), indicating the effectiveness of our strategy in enhancing the power output of ZBFB. These results demonstrate that CZGFs can not only promote dendrite-free Zn deposition but also enhance the reaction kinetics of the Br_2/Br^- reaction, thereby boosting the operating current density and cycle life of ZBFBs, which will unlock the potential of ZBFBs for grid-scale energy storage applications.

3. CONCLUSIONS

In summary, a nitrogen-doped, multiscale porous electrode has been successfully developed to simultaneously address the challenges of Zn shedding and sluggish Br_2/Br^- reaction kinetics in ZBFBs. DFT calculations reveal that the incorporation of *N*-containing functional groups can boost the adsorption of Zn atoms and Br_2 molecules to the carbon electrode, thereby achieving uniform and compact Zn deposition and fast bromine reaction kinetics. Phase field simulation demonstrates that rough electrode surfaces can enhance the mass transfer of Zn^{2+} ions, further promoting dendrite-free Zn deposition. Meanwhile, the CZGF electrodes also offer large specific surface area, providing more reaction sites for both positive and negative reactions. As a result, ZBFB using CZGF-1000 electrodes can achieve an EE of 68.0% at an ultrahigh current density of 250 mA cm^{-2}, which is 17.3% higher than that of the battery equipped with PGF electrodes. Moreover, the ZBFBs exhibit excellent stability and can survive more than 800 and 2000 cycles with no obvious degradation at 250 and 100 mA cm^{-2}, respectively. These results demonstrate that the newly designed electrodes can effectively address the key challenges in ZBFBs, representing a critical step toward development of high-performance ZBFBs for grid-scale energy storage.

https://doi.org/10.1021/acsami.4c22329
ACS Appl. Mater. Interfaces 2025, 17, 25206−25215

4. MATERIALS AND METHODS

4.1. Preparation of CZGF Electrodes. The GFs were purchased from the SGL carbon group, Germany. The GFs were cut into pieces of 2 × 2 cm^2, rinsed with absolute ethanol (EtOH, 99.9%, Anaqua) and deionized (DI) water, and oven-dried at 65 °C. ZIF-8 was synthesized based on reported methods with slight adjustments.[61,62] Specifically, 2.38 g of $Zn(NO_3)_2{\cdot}6H_2O$ (99%, Aladdin) and 5.2544 g of 2-methylimidazole (98%, Aladdin) were dissolved in 40 mL of absolute methanol (MeOH, 99.8%, Anaqua) followed by ultrasonication for 30 min. The solutions were mixed, magnetically stirred for 5 min, and then immersed with GFs under continuous stirring for 12 h. The obtained GFs were thoroughly washed with EtOH. The above procedures were repeated three times. Then, the ZGFs were dried at 65 °C. The prepared ZGFs were transferred to a quartz tube furnace (OTF-1200X, Hefei Kejing) and heated to 700, 800, 900, and 1000 °C under N_2 flow for 5 h. The ramp rate was set to 5 °C/min. Finally, the CZGFs were collected after cooling to ambient temperature.

4.2. Material Characterizations. The surface morphologies of different electrodes were observed by field-emission scanning electron microscopy (VEGA3). The crystal phase was analyzed via X-ray diffraction patterns obtained by an X-ray diffractometer (Rigaku SmartLab) with Cu Kβ radiation at 45 kV. The composition and chemical state of the prepared electrodes were determined by XPS (K-Alpha, Thermo Scientific). Raman spectra were collected with a WITec alpha300R Raman spectrometer. The specific surface area and pore size distribution of the samples were obtained by BET measurement (Micromeritics ASAP 2020).

4.3. Electrochemical Measurements. CV and EIS tests were conducted in a 0.1 M $ZnBr_2$ solution with a typical three-electrode cell configuration on a BioLogic electrochemical workstation. Different GFs with a geometric area of 1 cm^2, Ag/AgCl electrode with a salt bridge, and a Zn foil were employed as the working, reference, and counter electrode, respectively. CV tests were conducted with potential ranges of 0−1 V (vs Ag/AgCl) for the positive side and 0 to −1.2 V (vs Ag/AgCl) for the negative side at 10 mV s^{-1}. The EIS test was performed from 1 × 10^5 to 1 × 10^{-1} Hz with an amplitude of 10 mV. Charge−discharge performances of ZBFBs were assessed using a NEWARE battery test system. A Nafion 212 membrane was adopted as the separator, while 12.5 mL of solutions (1 M $ZnBr_2$ + 4 M NH_4Cl) were used as both negolyte and posolyte.

4.4. Computational Methods. The ABINIT code was employed for DFT calculations.[63] Core electrons were treated with the projector augmented wave method, utilizing a plane-wave basis set with a 22 Ha energy cutoff.[64] A 15 Å vacuum layer was applied in the slab model to avoid the influence of periodic interaction. The computational model consisted of a 4 × 4 × 1 supercell of graphite (0001) monolayer, and *K*-point Monkhorst−Pack grids of 4 × 4 × 1 were selected to sample the Brillouin zone.[65] Geometry optimization convergence criteria were set to 4 × 10^{-5} Ha $Bohr^{-1}$ for energy and 4 × 10^{-4} Ha $Bohr^{-1}$ for atomic forces.

The adsorption energies (E_{abs}) were calculated as the following formulas

$$\text{for Zn:} \quad E_{abs} = E_{total} - E_{Zn} - E_{substrate}$$

$$\text{for } Br_2\text{:} \quad E_{abs} = E_{total} - E_{Br_2} - E_{substrate}$$

where E_{total}, E_{Zn}, E_{Br_2}, and $E_{substrate}$ represent the energies of the whole system, Zn atom, Br_2 molecule and different substrate surfaces, respectively.

4.5. Phase Field Simulations. The dynamic morphological evolutions of Zn electrodeposition on the surfaces of both PGF and CZGF fibers are shown by phase field simulations. The modeling was based on published methods with modifications of the parameters used in the simulation.[66] The surfaces of PGF and CZGF were constructed based on SEM morphologies. The PGF surface is smooth, while the surface of CZGF has uniform continuous protrusions. The non-conserved order parameter (ξ) tracked phase transitions, where $\xi = 1$ represents the solid phase, $\xi = 0$ corresponds to the liquid phase, and the intermediate values ($0 < \xi < 1$) denote the transitional interface.[67] The relevant phase field simulation parameters for zinc deposition in ZBFB are summarized in Table S2.

■ ASSOCIATED CONTENT

Supporting Information

The Supporting Information is available free of charge at https://pubs.acs.org/doi/10.1021/acsami.4c22329.

Flow velocity distribution on the PGF and CZGF surface, and comparison of flow velocity between PGF and CZGF (Figure S1); schematic diagram of the preparation procedure of the CZGF electrodes (Figure S2); SEM images of ZIF-8 particles and ZIF-8 modified graphite felt at different magnifications (Figure S3); XRD patterns of PGF, ZIF-8 particles, ZGF, and CZGF carbonized at different temperatures (Figure S4); SEM images of CZGF-800, CZGF-900, and CZGF-1000 electrodes at different magnifications (Figure S5); full XPS spectra of CZGF-700 (Figure S6); full XPS spectra and N 1s XPS spectra of CZGF-1000 (Figure S7); pore size distribution curves of CZGF electrodes (Figure S8); CV profiles tested from 0 to −1.2 V vs Ag/AgCl and enlarged CV profiles of different samples (Figure S9); cycling performance of ZBFB using CZGF-1000 as the anode and PGF as the cathode at 100 mA cm^{-2}(Figure S10); SEM images of zinc deposited on PGF and CZGF-1000 negative electrode at different magnifications after being charged at 100 mA cm^{-2} and 40 mAh cm^{-2} (Figure S11); equivalent circuits of the EIS test (Figure S12); GCD curves of ZBFBs with both PGF and CZGF-1000 (Figure S13); polarization curve and power density of the ZBFB with both PGF and CZGF-1000 electrodes (Figure S14); comparison of ZBFB performance of this work and other related works using modified electrodes (Table S1); relevant parameters of the phase field simulation model (Table S2); and abbreviations of all acronyms given in the manuscript (Table S3) (PDF)

Phase field simulation of the Zn deposition process on the PGF electrode surface (MP4)

Phase field simulation of the Zn deposition process on the designed CZGF electrode surface (MP4)

■ AUTHOR INFORMATION

Corresponding Author

Maochun Wu − *Department of Mechanical Engineering, The Hong Kong Polytechnic University, Kowloon 999077 Hong Kong SAR, China*; orcid.org/0000-0002-8255-7827; Email: maochun.wu@polyu.edu.hk

Authors

Jiayi Li − *Department of Mechanical Engineering, The Hong Kong Polytechnic University, Kowloon 999077 Hong Kong SAR, China*

Zeyu Xu − *Department of Mechanical Engineering, The Hong Kong Polytechnic University, Kowloon 999077 Hong Kong SAR, China*

Complete contact information is available at: https://pubs.acs.org/10.1021/acsami.4c22329

Author Contributions

†J.L. and Z.X. contributed equally to this work. J.L.: Conceptualization, methodology, validation, formal analysis, investigation, data curation, visualization, and writing—original

https://doi.org/10.1021/acsami.4c22329
ACS Appl. Mater. Interfaces 2025, 17, 25206−25215

draft; Z.X.: simulation and calculation, formal analysis, methodology, investigation, and writing—review and editing; M.W.: writing—review and editing, resources, supervision, funding acquisition. All authors agreed with the final version of the manuscript.

Notes

The authors declare no competing financial interest.

■ ACKNOWLEDGMENTS

The work described in this paper was fully supported by the grant from the Research Grants Council of the Hong Kong Special Administrative Region, China (Project No. 25232523).

■ REFERENCES

(1) Soloveichik, G. L. Flow Batteries: Current Status and Trends. *Chem. Rev.* **2015**, *115*, 11533−11558.
(2) Li, Z.; Lu, Y. C. Polysulfide-Based Redox Flow Batteries with Long Life and Low Levelized Cost Enabled by Charge-Reinforced Ion-Selective Membranes. *Nat. Energy* **2021**, *6*, 517−528.
(3) Li, Z.; Lu, Y. C. Material Design of Aqueous Redox Flow Batteries: Fundamental Challenges and Mitigation Strategies. *Adv. Mater.* **2020**, *32*, No. 2002132.
(4) Wang, R.; Li, Y. Carbon Electrodes Improving Electrochemical Activity and Enhancing Mass and Charge Transports in Aqueous Flow Battery: Status and Perspective. *Energy Storage Mater.* **2020**, *31*, 230−251.
(5) Li, A.; Li, J.; He, Y.; Wu, M. Toward Stable and Highly Reversible Zinc Anodes for Aqueous Batteries via Electrolyte Engineering. *J. Energy Chem.* **2023**, *83*, 209−228.
(6) Li, J.; Xu, Z.; Wu, M. Halogen Enabled Aqueous Flow Cells for Large-Scale Energy Storage: Current Status and Perspectives. *J. Power Sources* **2023**, *581*, No. 233477.
(7) Wang, R.; Hao, M.; He, C.; Tu, Z.; Chong, F.; Li, Y. Gradient-Distributed $NiCo_2O_4$ Nanorod Electrode for Redox Flow Batteries: Establishing the Ordered Reaction Interface to Meet the Anisotropic Mass Transport. *Appl. Catal., B* **2023**, *332*, No. 122773.
(8) Sun, J.; Guo, Z.; Pan, L.; Fan, X.; Wei, L.; Zhao, T. Redox Flow Batteries and Their Stack-Scale Flow Fields. *Carbon Neutrality* **2023**, *2*, No. 30.
(9) Zhao, Y.; Ding, Y.; Li, Y.; Peng, L.; Byon, H. R.; Goodenough, J. B.; Yu, G. A Chemistry and Material Perspective on Lithium Redox Flow Batteries towards High-Density Electrical Energy Storage. *Chem. Soc. Rev.* **2015**, *44*, 7968−7996.
(10) Wang, C.; Lai, Q.; Xu, P.; Zheng, D.; Li, X.; Zhang, H. Cage-Like Porous Carbon with Superhigh Activity and Br_2-Complex-Entrapping Capability for Bromine-Based Flow Batteries. *Adv. Mater.* **2017**, *29*, No. 1605815.
(11) Xu, Z.; Wang, J.; Yan, S. C.; Fan, Q.; Lund, P. D. Modeling of Zinc Bromine Redox Flow Battery with Application to Channel Design. *J. Power Sources* **2020**, *450*, No. 227436.
(12) Wang, C.; Lu, W.; Lai, Q.; Xu, P.; Zhang, H.; Li, X. A TiN Nanorod Array 3D Hierarchical Composite Electrode for Ultrahigh-Power-Density Bromine-Based Flow Batteries. *Adv. Mater.* **2019**, *31*, No. 1904690.
(13) Guo, L.; Guo, H.; Huang, H.; Tao, S.; Cheng, Y. Inhibition of Zinc Dendrites in Zinc-Based Flow Batteries. *Front. Chem.* **2020**, *8*, No. 557.
(14) Heo, J.; Shin, K.; Kim, H. T. A Zinc−Bromine Battery with Deep Eutectic Electrolytes. *Adv. Sci.* **2022**, *9*, No. 2204908.
(15) Xu, Z.; Fan, Q.; Li, Y.; Wang, J.; Lund, P. D. Review of Zinc Dendrite Formation in Zinc Bromine Redox Flow Battery. *Renewable Sustainable Energy Rev.* **2020**, *127*, No. 109838.
(16) Xue, J.; Deng, S.; Wang, R.; Li, Y. Efficient Synergistic Effect of Trimetallic Organic Frameworks Derived as Bifunctional Catalysis for the Rechargeable Zinc-Air Flow Battery. *Carbon* **2023**, *205*, 422−434.
(17) Xu, N.; Yuan, C.; Sun, G.; Chen, N.; Yao, S.; Du, F. Na5YSi4O12 Fast Ion Conductor Protection Layer Enabled Dendrite-Free Zn Metal Anode. *Carbon Neutrality* **2023**, *2*, No. 33.
(18) Suresh, S.; Ulaganathan, M.; Aswathy, R.; Ragupathy, P. Enhancement of Bromine Reversibility Using Chemically Modified Electrodes and Their Applications in Zinc Bromine Hybrid Redox Flow Batteries. *ChemElectroChem* **2018**, *5*, 3411−3418.
(19) Tang, L.; Li, T.; Lu, W.; Li, X. Lamella-like Electrode with High Br_2-Entrapping Capability and Activity Enabled by Adsorption and Spatial Confinement Effects for Bromine-Based Flow Battery. *Sci. Bull.* **2022**, *67*, 1362−1371.
(20) Sun, Y.; Zhang, S.; Zhang, Q.; Cui, L.; Wang, P.; Yin, Y.; Wang, Q.; Lai, Q. Enlarging Zn Deposition Space via Regulating Sn-Induced Effective Interface for High Areal Capacity Zinc-Based Flow Battery. *J. Energy Chem.* **2023**, *86*, 579−586.
(21) Lu, W.; Xu, P.; Shao, S.; Li, T.; Zhang, H.; Li, X. Multifunctional Carbon Felt Electrode with N-Rich Defects Enables a Long-Cycle Zinc-Bromine Flow Battery with Ultrahigh Power Density. *Adv. Funct. Mater.* **2021**, *31*, No. 2102913.
(22) Sun, J.; Jiang, H. R.; Zhang, B. W.; Chao, C. Y. H.; Zhao, T. S. Towards Uniform Distributions of Reactants via the Aligned Electrode Design for Vanadium Redox Flow Batteries. *Appl. Energy* **2020**, *259*, No. 114198.
(23) Lee, J. H.; Kim, R.; Kim, S.; Heo, J.; Kwon, H.; Yang, J. H.; Kim, H. T. Dendrite-Free Zn Electrodeposition Triggered by Interatomic Orbital Hybridization of Zn and Single Vacancy Carbon Defects for Aqueous Zn-Based Flow Batteries. *Energy Environ. Sci.* **2020**, *13*, 2839−2848.
(24) Yin, Y.; Wang, S.; Zhang, Q.; Song, Y.; Chang, N.; Pan, Y.; Zhang, H.; Li, X. Dendrite-Free Zinc Deposition Induced by Tin-Modified Multifunctional 3D Host for Stable Zinc-Based Flow Battery. *Adv. Mater.* **2020**, *32*, No. 1906803.
(25) Xiang, H. X.; Tan, A. D.; Piao, J. H.; Fu, Z. Y.; Liang, Z. X. Efficient Nitrogen-Doped Carbon for Zinc−Bromine Flow Battery. *Small* **2019**, *15*, No. 1901848.
(26) Mariyappan, K.; Ragupathy, P.; Ulaganathan, M. Enhancement of Bromine Kinetics Using Pt@Graphite Felt and Its Applications in Zn-Br_2 Redox Flow Battery. *J. Electrochem. Soc.* **2021**, *168*, No. 090566.
(27) Munaiah, Y.; Suresh, S.; Dheenadayalan, S.; Pillai, V. K.; Ragupathy, P. Comparative Electrocatalytic Performance of Single-Walled and Multiwalled Carbon Nanotubes for Zinc Bromine Redox Flow Batteries. *J. Phys. Chem. C* **2014**, *118*, 14795−14804.
(28) Yang, M.; Xu, Z.; Xiang, W.; Xu, H.; Ding, M.; Li, L.; Tang, A.; Gao, R.; Zhou, G.; Jia, C. High Performance and Long Cycle Life Neutral Zinc-Iron Flow Batteries Enabled by Zinc-Bromide Complexation. *Energy Storage Mater.* **2022**, *44*, 433−440.
(29) Wang, S.; Wang, Z.; Yin, Y.; Li, T.; Chang, N.; Fan, F.; Zhang, H.; Li, X. A Highly Reversible Zinc Deposition for Flow Batteries Regulated by Critical Concentration Induced Nucleation. *Energy Environ. Sci.* **2021**, *14*, 4077−4084.
(30) Yang, Q.; Li, Q.; Liu, Z.; Wang, D.; Guo, Y.; Li, X.; Tang, Y.; Li, H.; Dong, B.; Zhi, C. Dendrites in Zn-Based Batteries. *Adv. Mater.* **2020**, *32*, No. 2001854.
(31) Fu, Y.; Wei, Q.; Zhang, G.; Wang, X.; Zhang, J.; Hu, Y.; Wang, D.; Zuin, L.; Zhou, T.; Wu, Y.; Sun, S. High-Performance Reversible Aqueous Zn-Ion Battery Based on Porous MnO_x Nanorods Coated by MOF-Derived N-Doped Carbon. *Adv. Energy Mater.* **2018**, *8*, No. 1801445.
(32) Zhou, J.; Xie, M.; Wu, F.; Mei, Y.; Hao, Y.; Huang, R.; Wei, G.; Liu, A.; Li, L.; Chen, R. Ultrathin Surface Coating of Nitrogen-Doped Graphene Enables Stable Zinc Anodes for Aqueous Zinc-Ion Batteries. *Adv. Mater.* **2021**, *33*, No. 2101649.
(33) Cao, Q.; Gao, H.; Gao, Y.; Yang, J.; Li, C.; Pu, J.; Du, J.; Yang, J.; Cai, D.; Pan, Z.; Guan, C.; Huang, W. Regulating Dendrite-Free Zinc Deposition by 3D Zincopilic Nitrogen-Doped Vertical Graphene for High-Performance Flexible Zn-Ion Batteries. *Adv. Funct. Mater.* **2021**, *31*, No. 2103922.
(34) Mofokeng, T. P.; Tetana, Z. N.; Ozoemena, K. I. Defective 3D Nitrogen-Doped Carbon Nanotube-Carbon Fibre Networks for High-

https://doi.org/10.1021/acsami.4c22329
ACS Appl. Mater. Interfaces 2025, 17, 25206−25215

Performance Supercapacitor: Transformative Role of Nitrogen-Doping from Surface-Confined to Diffusive Kinetics. *Carbon* **2020**, *169*, 312−326.
(35) Xu, X.; Xu, Y.; Zhang, J.; Zhong, Y.; Li, Z.; Qiu, H.; Wu, H. B.; Wang, J.; Wang, X.; Gu, C.; Tu, J. Quasi-Solid Electrolyte Interphase Boosting Charge and Mass Transfer for Dendrite-Free Zinc Battery. *Nano-Micro Lett.* **2023**, *15*, No. 56.
(36) Gao, Y.; Qiao, F.; You, J.; Shen, C.; Zhao, H.; Gu, J.; Ren, Z.; Xie, K.; Wei, B. Regulating Electrodeposition Behavior through Enhanced Mass Transfer for Stable Lithium Metal Anodes. *J. Energy Chem.* **2021**, *55*, 580−587.
(37) Kim, J.; Park, H. Recent Advances in Porous Electrodes for Vanadium Redox Flow Batteries in Grid-Scale Energy Storage Systems: A Mass Transfer Perspective. *J. Power Sources* **2022**, *545*, No. 231904.
(38) Park, K. S.; Ni, Z.; Côté, A. P.; Choi, J. Y.; Huang, R.; Uribe-Romo, F. J.; Chae, H. K.; O'Keeffe, M.; Yaghi, O. M. Exceptional Chemical and Thermal Stability of Zeolitic Imidazolate Frameworks. *Proc. Natl. Acad. Sci. U.S.A.* **2006**, *103*, 10186−10191.
(39) Chhetri, K.; Tiwari, A. P.; Dahal, B.; Ojha, G. P.; Mukhiya, T.; Lee, M.; Kim, T.; Chae, S. H.; Muthurasu, A.; Kim, H. Y. A ZIF-8-Derived Nanoporous Carbon Nanocomposite Wrapped with Co_3O_4-Polyaniline as an Efficient Electrode Material for an Asymmetric Supercapacitor. *J. Electroanal. Chem.* **2020**, *856*, No. 113670.
(40) Zhang, L.; Su, Z.; Jiang, F.; Yang, L.; Qian, J.; Zhou, Y.; Li, W.; Hong, M. Highly Graphitized Nitrogen-Doped Porous Carbon Nanopolyhedra Derived from ZIF-8 Nanocrystals as Efficient Electrocatalysts for Oxygen Reduction Reactions. *Nanoscale* **2014**, *6*, 6590−6602.
(41) Xu, Z.; Zhu, M.; Zhang, K.; Zhang, X.; Xu, L.; Liu, J.; Liu, T.; Yan, C. Inspired by "Quenching-Cracking" Strategy: Structure-Based Design of Sulfur-Doped Graphite Felts for Ultrahigh-Rate Vanadium Redox Flow Batteries. *Energy Storage Mater.* **2021**, *39*, 166−175.
(42) Ganesan, K.; Ghosh, S.; Gopala Krishna, N.; Ilango, S.; Kamruddin, M.; Tyagi, A. K. A Comparative Study on Defect Estimation Using XPS and Raman Spectroscopy in Few Layer Nanographitic Structures. *Phys. Chem. Chem. Phys.* **2016**, *18*, 22160−22167.
(43) Abbasi, Z.; Shamsaei, E.; Kwan, S.; Ladewig, B.; Zhang, X.; Wang, H. Effect of Carbonization Temperature on Adsorption Property of ZIF-8 Derived Nanoporous Carbon for Water Treatment. *Microporous Mesoporous Mater.* **2016**, *236*, 28−37.
(44) Liu, Y.; Xu, X.; Wang, M.; Lu, T.; Sun, Z.; Pan, L. Metal − Organic Framework-Derived Porous Carbon Polyhedra for Highly Efficient Capacitive. *Chem. Commun.* **2015**, *51*, 12020−12023.
(45) Xiao, Y.; Yang, H.; Bu, X.; Feng, P. ZIF-8 Derived Carbon Materials with Multifunctional Selective Adsorption Abilities. *Carbon* **2021**, *176*, 421−430.
(46) Chen, A.; Cheng, M.; Huang, D.; Zhang, G.; Wang, W.; Du, L.; Wang, G.; Liu, H.; Chen, Y.; Xiao, W.; Shi, Q. Versatile Metal-Free Carbon Materials from ZIF-8: Insights into Construction Strategies, Properties, Applications and Structure-Activity Relationships. *Renewable Sustainable Energy Rev.* **2024**, *199*, No. 114520.
(47) Mel'gunov, M. S. Application of the Simple Bayesian Classifier for the N_2 (77 K) Adsorption/Desorption Hysteresis Loop Recognition. *Adsorption* **2023**, *29*, 199−208.
(48) Luo, X.; Zhou, M.; Luo, Z.; Shi, T.; Li, L.; Xie, X.; Sun, Y.; Cao, X.; Long, M.; Liang, S.; Fang, G. Regulation of Desolvation Process and Dense Electrocrystalization Behavior for Stable Zn Metal Anode. *Energy Storage Mater.* **2023**, *57*, 628−638.
(49) Jian, Q.; Guo, Z.; Zhang, L.; Wu, M.; Zhao, T. A Hierarchical Porous Tin Host for Dendrite-Free, Highly Reversible Zinc Anodes. *Chem. Eng. J.* **2021**, *425*, No. 130643.
(50) Li, A.; Zhang, X.; Xu, Z.; Wu, M. Non-Sacrificial Additive Regulated Electrode−Electrolyte Interface Enables Long-Life, Deeply Rechargeable Aqueous Zn Anodes. *Chem. Eng. J.* **2024**, *494*, No. 153240.
(51) Xu, Z.; Li, J.; Wu, M. A High-Rate and Long-Life Zinc-Bromine Flow Battery. *J. Power Sources* **2024**, *613*, No. 234869.
(52) Sun, J.; Zeng, L.; Jiang, H. R.; Chao, C. Y. H.; Zhao, T. S. Formation of Electrodes by Self-Assembling Porous Carbon Fibers into Bundles for Vanadium Redox Flow Batteries. *J. Power Sources* **2018**, *405*, 106−113.
(53) Zhang, Q.; Jiang, H.; Liu, S.; Wang, Q.; Wang, J.; Zhou, Z.; Cai, K.; Lai, Q.; Wang, Q. Redox-Targeting Catalyst Developing New Reaction Path for High-Power Zinc-Bromine Flow Batteries. *J. Power Sources* **2024**, *601*, No. 234286.
(54) Mariyappan, K.; Mahalakshmi, T.; Roshni, T. S.; Ragupathy, P.; Ulaganathan, M. Nanocatalyzed PtNi Alloy Intact @3D Graphite Felt as an Effective Electrode for Super Power Redox Flow Battery. *Adv. Mater. Interfaces* **2023**, *10*, No. 2202007.
(55) Tang, L.; Liao, C.; Li, T.; Yuan, C.; Li, G.; Lu, W.; Li, X. In Situ Vertically Aligned MoS_2 Arrays Electrodes for Complexing Agent-Free Bromine-Based Flow Batteries with High Power Density and Long Lifespan. *Adv. Energy Mater.* **2024**, *14*, No. 2303282.
(56) Mariyappan, K.; Saravanakumar, P.; Thamizhselvan, R.; Ragupathy, P.; Ulaganathan, M. In-Situ N-RGO Scaffold @3D Graphite Felt for High Power Polyhalide Hybrid Redox Flow Battery. *Adv. Mater. Technol.* **2023**, *8*, No. 2200869.
(57) Naresh, R.; Velmurugan, R.; Subramanian, B.; Ragupathy, P. Laser Ablated Uniform Deposition of Bismuth Oxide Film as Efficient Anode for Zinc Based Flow Battery. *Electrochim. Acta* **2023**, *451*, No. 142287.
(58) Jung, H. J.; Lee, J. H.; Park, J. Y.; Shin, K.; Kim, H. T.; Cho, E. A. A Mesoporous Tungsten Oxynitride Nanofibers/Graphite Felt Composite Electrode with High Catalytic Activity for the Cathode in Zn-Br Flow Battery. *Small* **2023**, *19*, No. 2208280.
(59) Lai, Q.; Liu, S.; Jiang, H.; Zhang, J.; Zhou, Z.; Wang, J.; Wang, Q.; Wang, Q. Urchin-Like Mesoporous TiN Hollow Sphere Enabling Promoted Electrochemical Kinetics of Bromine-Based Flow Batteries. *Small* **2024**, *20*, No. 2309712.
(60) Zhang, S.; Jiang, H.; Liu, S.; Zhou, Z.; Wang, J.; Wang, Q.; Cai, K.; Lai, Q.; Wang, Q. Regulated Adsorption Capability by Interface−Electric−Field Enabling Promoted Electrochemical Kinetics of Zinc−Bromine Flow Batteries. *Chem. Eng. J.* **2024**, *486*, No. 150317.
(61) Lee, J. H.; Byun, Y.; Jeong, G. H.; Choi, C.; Kwen, J.; Kim, R.; Kim, I. H.; Kim, S. O.; Kim, H. T. High-Energy Efficiency Membraneless Flowless Zn−Br Battery: Utilizing the Electrochemical−Chemical Growth of Polybromides. *Adv. Mater.* **2019**, *31*, No. 1904524.
(62) Yu, F.; Wang, L.; Ma, H.; Pan, Y. Zeolitic Imidazolate Framework-8 Modified Active Carbon Fiber as an Efficient Cathode in Electro-Fenton for Tetracycline Degradation. *Sep. Purif. Technol.* **2020**, *237*, No. 116342.
(63) Jiang, H. R.; Shyy, W.; Zeng, L.; Zhang, R. H.; Zhao, T. S. Highly Efficient and Ultra-Stable Boron-Doped Graphite Felt Electrodes for Vanadium Redox Flow Batteries. *J. Mater. Chem. A* **2018**, *6*, 13244−13253.
(64) Jiang, H. R.; Zeng, Y. K.; Wu, M. C.; Shyy, W.; Zhao, T. S. A Uniformly Distributed Bismuth Nanoparticle-Modified Carbon Cloth Electrode for Vanadium Redox Flow Batteries. *Appl. Energy* **2019**, *240*, 226−235.
(65) Wang, R.; Li, Y.; Wang, Y.; Fang, Z. Phosphorus-Doped Graphite Felt Allowing Stabilized Electrochemical Interface and Hierarchical Pore Structure for Redox Flow Battery. *Appl. Energy* **2020**, *261*, No. 114369.
(66) Jian, Q.; Sun, J.; Li, H.; Guo, Z.; Zhao, T. Phase-Field Modeling of Zinc Dendrites Growth in Aqueous Zinc Batteries. *Int. J. Heat Mass Transfer* **2024**, *223*, No. 125252.
(67) Hong, Z.; Viswanathan, V. Phase-Field Simulations of Lithium Dendrite Growth with Open-Source Software. *ACS Energy Lett.* **2018**, *3*, 1737−1743.

https://doi.org/10.1021/acsami.4c22329
ACS Appl. Mater. Interfaces 2025, 17, 25206−25215